Planetary Entry Descent Mission Design Tool

Abinay J. Brown
Georgia Institute of Technology, Atlanta, Georgia, 30332

This paper presents the development of a Planetary Entry Descent mission design tool for simulating atmospheric reentry trajectories, estimating deorbiting parameters, calculating heating rates and loads experienced by spacecraft under varying entry conditions, and performing parametric variational analysis and Monte Carlo runs to quantify landing errors. The tool employs 3DOF planar and nonplanar equations of motion with atmospheric and gravity models, and the Sutton-Graves correlation for heating calculations. Validation was performed using the Stardust and Viking missions as test cases. The tool effectively predicted entry trajectories, accurately estimating entry corridors and a flight path angle of 8° at 10.5 km/s, with only a 2% error in peak deceleration results. Heating rates were overestimated due to varying coefficients. The Viking mission simulation also closely matched reference trajectories. The tool's Monte Carlo simulations generated landing ellipses consistent in shape with reference data. Future improvements include higher-order integrators, updated models, and extending capabilities to hyperbolic entries. This tool provides a robust foundation for EDL analysis in planetary missions.

I. Nomenclature

m	=	Mass
L	=	Lift force
D	=	Drag force
C_{pmax}	=	Newtonian Pressure Coefficient
C_L	=	Lift Coefficient
C_D	=	Drag coefficient
C_N	=	Normal Force coefficient
C_A	=	Axial Force coefficient
α	=	Angle of attack
δ	=	Cone Angle
ρ	=	Atmospheric density
β	=	Ballistic coefficient
$\bar{R}$	=	Universal Gas constant
M_{w0}	=	Molecular Weight
P	=	Pressure
T	=	Temperature
T_m	=	Molecular scale temperature
L_h	=	Molecular Scale Lapse Rate
r_n	=	nose radius
r_c	=	cone radius
V	=	Velocity
h	=	Height
γ	=	Flight Path Angle
σ	=	Bank Angle
ψ	=	Azimuth angle
ϕ	=	Latitude
θ	=	Longitude
ω	=	Planet Angular Velocity
ν	=	True Anomaly

r	=	Radius
e	=	eccentricity
p	=	Semi-Latus Rectum
a	=	Semi-Major Axis
h	=	Angular Momentum
λ	=	Non-Dimensionalized radius
u	=	Non-Dimensionalized velocity
g	=	Gravitational acceleration
μ	=	Planet Gravitational parameter
J_2	=	Planet J2 Coefficient
K	=	Planet ellipticity
Re	=	Planet Radius
Req	=	Planet Equatorial Radius
P	=	Pressure
H	=	Scale height
Z	=	Geometric height

II. Introduction

Entry and Descent are critical phases in missions aimed at exploring other planets, as well as missions traveling to space and returning to Earth. These phases involve complex dynamics and interactions with the atmosphere that must be accurately predicted to ensure mission success. From the Apollo missions [1] that brought astronauts to the moon and back, to the earliest Viking missions [2] that landed on Mars, the entry descent phases have been crucial to achieving mission objectives. These phases are filled with challenges, for example, extreme atmospheric-heating that could burn up the vehicle into ashes, high velocity maneuvers that can damage the vehicle/mission by pulling higher g's than its design for or even reaching a different orbit instead of reentrying the atmosphere leading to a mission failure.

The significance of accurately modeling and simulating entry descent phases are crucial for space mission as ensuring the safety of both the entry vehicle and any potential crew or scientific payloads is paramount, as any errors in these phase can result in mission failure. Furthermore, optimizing entry descent phases can save fuel and other resources, which is critical for long-duration missions.

In this research project, we develop a mission design tool aimed at simulating atmospheric reentry trajectories, estimating deorbiting parameters and entry corridors, as well as calculating the heating rates and loads experience by the spacecraft at varying entry conditions. This is done by integrating planar and non-planar equations of motion[3] with atmospheric and gravity models to develop the trajectory, and the use of the Sutton-Graves correlation [4] for the heating. The deorbit parameters are estimated using orbital mechanics equations. In addition to this, Monte Carlo Runs as well as Lift and Bank Modulating analysis can be run to determine landing accuracy in the presence of errors in the entry conditions, as well as determining cross-range and downrange results distances. To validate the efficacy of the tool, the Stardust mission as well as the Viking mission are used as test cases to determine its accuracy.

III. Methodology

The tool implements planar and nonplanar equations of motions; planar EOM used for basic analysis that includes entry corridor determination, nominal trajectory and heating profile generation, as well as parameter variational analysis. The non-planar EOM in addition to the same capabilities can perform Monte-Carlo Analysis for landing ellipse generation, lift modulation, downrange and cross range determination. Designing an entry descent phases of the mission planning requires information on the deorbit parameters, atmospheric models, gravity models, vehicle geometry, and 3DOF equations of motions based on the fidelity of the simulation and the type of analysis required. The following subsections detail the implementation of these mission parameters that can be used in the tool as required.

A. 3DOF Equations of Motion

The tool uses planar as well as non-planar equations of motion to generate the trajectory, the simulation assumes a ballistic entry, zero angle of attack, with the ability to specify alpha to determine the LD ratio, this is used in the parameter analysis sections. In this simulation, a simple constant step size Runge-Kutta 4th order integrator is used for integration, this is because of the restrictions and issues that are faced in using predefined functions such as ode45 and ode113 with converging with step-sizes especially if the trajectory skips-off without reentering or error tolerance convergence when random errors are introduced for the Monte-Carlo Runs.

1. Planar

The planar equations of motion used in the simulation tool are given by the equations below[5]. It is important to note that these EOM are limited to only using the simple inverse-square law gravity model.

$$\frac{dV}{dt} = \frac{-\rho V^2}{2\beta} + g\sin(\gamma) \tag{1}$$

$$V\frac{d\gamma}{dt} = \frac{-V^2\cos(\gamma)}{r} - \frac{\rho V^2 cos\sigma \frac{L}{D}}{2\beta} + gsin(\gamma) \tag{2}$$

$$\frac{dh}{dt} = -V\sin(\gamma) \tag{3}$$

2. Non-Planar

The non-planar equations of motion used in the simulation takes into account the earth's rotation, heading angle, latitude, and longitude, for a higher dimensional analysis[3]. For the case of the Non-planar equations, a more accurate: J2 gravity model is used for the simulation as it requires the use of latitude that is determined from integrating the equations of motions.

$$\frac{dV}{dt} = \frac{-D}{m} - g\sin\gamma + \omega^2 r\cos\theta\,(\sin\gamma\cos\theta - \cos\gamma\sin\theta\sin\psi) \tag{4}$$

$$V\frac{d\gamma}{dt} = \frac{L}{m}\cos\sigma - \left(g - \frac{V^2}{r}\right)\cos\gamma + 2\omega V\cos\theta\cos\psi + \omega^2 r\cos\theta\,(\cos\gamma\cos\theta + \sin\gamma\sin\theta\sin\psi) \tag{5}$$

$$V\cos\gamma\frac{d\psi}{dt} = \frac{L}{m}\frac{\sin\sigma}{\cos\gamma} - \frac{V^2}{r}\cos\gamma\cos\psi\tan\theta + 2\omega V(\tan\gamma\cos\theta\sin\psi - \sin\theta) - \frac{\omega^2 r}{\cos\gamma}\sin\theta\cos\theta\cos\psi \tag{6}$$

$$\frac{dr}{dt} = V\sin\gamma \tag{7}$$

$$\frac{d\phi}{dt} = \frac{V\cos\gamma\cos\psi}{r\cos\theta} \tag{8}$$

$$\frac{d\theta}{dt} = \frac{V\cos\gamma\sin\psi}{r} \tag{9}$$

Where Drag and Lift Are determined from the Lift-Drag Ratio and the ballistic coefficient as shown below:

$$D = \frac{1}{2}\rho V^2\frac{m}{\beta} \tag{10}$$

$$L = \frac{1}{2}\rho V^2\left(\frac{L}{D}\right)\frac{m}{\beta} \tag{11}$$

B. Atmospheric Density Models

A simpler exponential atmospheric density model is adopted for entry into planetary bodies, for the case of Earth, a high fidelity 1976-1962 atmospheric model is also presented.

1. Exponential Atmosphere

The exponential atmospheric density model, derived under the assumptions of constant temperature and scale height, describes how atmospheric density decreases exponentially with altitude given the base density given by the equation below.

$$\rho = \rho_0 e^{-h/H} \tag{12}$$

2. 1976-1962 Earth's Atmosphere

For the case of Earth's Entry Descent, the tool has the ability to use the higher fidelty 1976 model[6] that ranges from 0 to 86km height and the 1962 model that ranges from 86 to 150km altitudes. The equations below are used in a piece-wise manner to determine the density based on the ranges of the Geopotential height from altitudes of 0 to 86km the parameters are determined from table 1 from the 1976 model[7]. The conversion from Geometric to Geopotential height h is given by Eqn 13. Additionally, this region assumes a constant Molecular Weight since it has negligible change below 86km and hence R = 287 J/(Kg.K). Equation 15 is used when the Molecular scale lapse rate is non-zero and equation16 is used in the altitude ranges with zero lapse rate. Finally Equation 17 is used to determine the density.

$$H = \frac{r_0 Z}{r_0 + Z} \tag{13}$$

$$T_m = T_{m_i} + L_{h_i}(h - h_i) \tag{14}$$

$$P = P_i \left[\frac{T_{m_i}}{T_{m_i} + L_{h_i}(h - h_i)} \right]^{\frac{g_0}{RL_{h_i}}} \tag{15}$$

$$P = P_i \exp \left[\frac{-g_0' M_{W0}(h - h_i)}{\overline{R} T_{m_i}} \right] \tag{16}$$

$$\rho = \frac{P M_{W_0}}{R T_m} \tag{17}$$

Table 1 1976 Atmosphere model for 0-86km altitude range

Region	Geopotential height, h_i (km)	Geometric height, Z (km)	Molecular Scale Lapse Rate, $L_{h,i}$ (K/km)	Molecular Scale Temperature $T_{m,i}$ (K)	Pressure P_i (N/m^2)
0	0-11	11.0102	-6.5	288.15	101325
1	11-20	20.0631	0.0	216.65	22631.95
2	20-32	32.1619	1.0	216.65	5474.79
3	32-47	47.3501	2.8	228.65	868.01
4	47-51	51.4125	0.0	270.65	110.9
5	51-71	71.8020	-2.8	270.65	66.94
6	71 - 84.852	86.0	-2.0	214.65	3.956

For altitudes above 86km and below 150km, the 1962 model is used to determine density from the piecewise parameters from table 2, in this region molecular weight varies drastically, in this case its interpolated from the data given in table 2 and used to normalize the gas constant $\bar{R} = 8.314 J/(mol.K)$ at every iteration by the updated molecular weight. The kinetic temperature is given by 14 and then similarly used below to determine the density given by eqn 18 where the exponent is given by equation 19.

$$\rho = \rho_i \left(\frac{T_m}{T_{m,i}}\right)^{[\text{pow}]_\rho} \exp\left[\frac{g_0 - b}{RL_{z,i}}(z - z_i)\right] \tag{18}$$

$$[\text{pow}]_\rho = -\left[\frac{g_0}{RL_{z,i}}\left(\frac{RL_{z,i}}{g_0} + 1 + b\left(\frac{T_{m,i}}{L_{z,i}} - z_i\right)\right)\right] \tag{19}$$

Table 2 1962 Earth Atmospheric for 86-150km altitude range

Region	Geometric height, Z (km)	Molecular Scale Lapse Rate, $L_{z,i}$ (K/km)	Molecular Temp $T_{m,i}$ (K)	Kinetic Temp T (K)	Molar Weight (kg/kmol)	Pressure P_i (N/m^2)
7	86 - 100	1.6481	186.945	186.946	28.9644	0.34313
8	100 - 110	5.0	210.65	210.02	28.88	0.030075
9	110 - 120	10.0	260.65	257.0	28.56	0.0073544
10	120 - 150	20.0	360.65	349.49	28.08	0.0025217

C. Gravity Models

1. Inverse-Square Law

The inverse square law gravity model simply uses the Newtonian gravity model that is based on the geometric height given by equation 20.

$$g = \frac{\mu}{r^2} \tag{20}$$

$$r = R + h \tag{21}$$

2. J2 Gravity Model

Due to Earth's oblateness effects due to equatorial bulge, it is more accurate to account for the J2 oblateness effects in calculating the local Earth radius and the gravitational acceleration as a function of latitude [8]. Equation 22 is used to determine the local Earth radius from the latitude and earth's ellipticity, this gives us the local distance r from center to the vehicle from eqn 23. Then equation 24 and 25 is used to find the local gravitational acceleration. It is important to note that the J2 model can only be used if the nonplanar equations of motions are used.

$$R = R_{eq}\left(1 - K\sin^2(\phi)\right) \tag{22}$$

$$r = R + h \tag{23}$$

$$D = K\left(1 - \frac{h}{R_e}\right)\sin(2\phi) \tag{24}$$

$$g = \left(\frac{\mu}{r^2}\right)\left(1 - \frac{3J_2}{4}\left(1 - 3\cos(2\phi)\right)\right) - r\omega^2\cos^2(\phi - D) \tag{25}$$

D. Vehicle Geometry

The tool has the ability to estimate the lift and drag coefficients of the vehicle based on the conic and biconic geometry parameters [9], the angle of attack, and the Cpmax of the flow. The tool by default assumes Newtonian flow, but by setting the Cpmax, modified Newtonian flow is applicable as well. For majority of the simulation demonstrated in this paper, a ballistic entry is assumed, zero angle-of-attack, hence zero lift, except for variational analysis or Lift and Drag modulation analysis.

1. Conic Axis-symmetric Blunt-Nose

The parameters and the geometry of the Axis-symmetric blunt-nose cone is shown in figure 1.

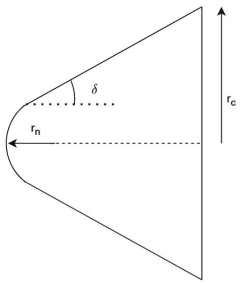

Fig. 1 Conic Vehicle Geometry

The equations to determine the normal and axial force coefficients and then the lift and drag coefficients as well as the area is given by equations 26 to 30.

$$C_N = C_{p_{\max}} \left(1 - \left(\frac{r_n}{r_c}\right)^2 \cos^2(\delta_c)\right) \left(\cos^2(\delta_c)\sin(\alpha)\cos(\alpha)\right) \tag{26}$$

$$C_A = C_{p_{\max}} \left(0.5\left(1 - \sin^4(\delta_c)\right)\left(\frac{r_n}{r_c}\right)^2 + \left(\sin^2(\delta_c)\cos^2(\alpha) + 0.5\sin^2(\alpha)\cos^2(\delta_c)\right)\left(1 - \left(\frac{r_n}{r_c}\right)^2 \cos^2(\delta_c)\right)\right) \tag{27}$$

$$C_L = C_N \cos(\alpha) - C_A \sin(\alpha) \tag{28}$$

$$C_D = C_N \sin(\alpha) + C_A \cos(\alpha) \tag{29}$$

$$A = \pi r_c^2 \tag{30}$$

2. Biconic Axis-symmetric Blunt-Nose

The parameters and the geometry of the Axis-symmetric blunt-nose cone is shown in figure 2.

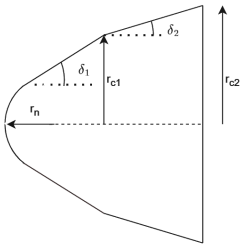

Fig. 2 Biconic Vehicle Geometry

Similarly, equations for finding the lift, drag, area of the biconic geometry are given by equations 31 to 40. First the geometry is split into three sections for which the normal and axial coefficients are found and then added after normalizing them by its area ratios.

$$C_{N1} = \frac{C_{p_{\max}}}{2r_{c1}^2}\left(r_{c1}^2 - (r_n\cos(\delta_1))^2\right)\sin(2\alpha)\cos^2(\delta_1) \tag{31}$$

$$C_{N2} = \frac{C_{p_{\max}}}{2r_{c2}^2}\left(r_{c2}^2 - r_{c1}^2\right)\sin(2\alpha)\cos^2(\delta_2) \tag{32}$$

$$C_N = \left(\frac{r_{c1}}{r_{c2}}\right)^2 C_{N1} + C_{N2} \tag{33}$$

$$C_{A_{\text{nose}}} = \frac{C_{p_{\max}}}{2}\left(1 - \sin^4(\delta_1)\right) \tag{34}$$

$$C_{A1} = \frac{C_{p_{\max}}}{2r_{c1}^2}\left(r_{c1}^2 - (r_n\cos(\delta_1))^2\right)\left((\cos(\delta_1)\sin(\alpha))^2 + 2(\cos(\alpha)\sin(\delta_1))^2\right) \tag{35}$$

$$C_{A2} = \frac{C_{p_{\max}}}{2r_{c2}^2}\left(r_{c2}^2 - r_{c1}^2\right)\left((\cos(\delta_2)\sin(\alpha))^2 + 2(\cos(\alpha)\sin(\delta_2))^2\right) \tag{36}$$

$$C_A = \left(\frac{r_n}{r_{c2}}\right)^2 C_{A_{\text{nose}}} + \left(\frac{r_{c1}}{r_{c2}}\right)^2 C_{A1} + C_{A2} \tag{37}$$

$$C_L = C_N\cos(\alpha) - C_A\sin(\alpha) \tag{38}$$

$$C_D = C_N\sin(\alpha) + C_A\cos(\alpha) \tag{39}$$

$$A = \pi r_{c2}^2 \tag{40}$$

E. Deorbit Trajectory Estimation

Given the Orbit parameters, the periapsis radius and the eccentricity of the orbit, equations 41 to 51 are used to estimate the entry velocity constraint u_e, a value slightly lower than this is taken to satisfy the constraint. It is important to note that to determine the minimum delta-V required for the maneuver, the true anomaly is taken as 180^0 by default.

$$a_1 = \frac{r_p}{1-e} \tag{41}$$

$$r_a = a_1(1+e) \tag{42}$$

$$\epsilon = -\frac{\mu}{2a_1} \tag{43}$$

$$p = a_1(1-e^2) \tag{44}$$

$$h = \sqrt{\mu p} \tag{45}$$

$$r_d = \frac{p}{1+e\cos(\nu)} \tag{46}$$

$$\lambda = \frac{r_d}{R_{atm}} \tag{47}$$

$$\alpha_1 = \frac{a_1}{R_{atm}} \tag{48}$$

$$u_1 = \sqrt{\frac{2\alpha_1 - \lambda}{\alpha_1}} \tag{49}$$

$$V_1 = u_1\sqrt{\frac{\mu}{r_d}} \tag{50}$$

$$u_e = \sqrt{\frac{2\lambda(\lambda-1)(1-e^2)\alpha_1^2}{(\lambda(1-e^2)\alpha_1^2) - 2\alpha_1 + \lambda}} \tag{51}$$

The flight path angle corridor is then solved for using bisection method where n_{max} is numerically solved until a flight path angle that nearly satisfies the n_{max} constraint specified by the user is found for the undershoot boundary. For the overshoot boundary bisection method is again used to find a flight path angle that is just lower than the grazing trajectory to ensure reentry.

Once the flight path angle corridor is found, if the entry velocity that was chosen earlier does not produce a γ that lies within the corridor, it is systematically lowered until the flight path angle is within the corridor. The 52 is used for estimating the γ as a function of the entry velocity.

$$\cos(\gamma_e) = \frac{\alpha_1}{u_e}\sqrt{\lambda(1-e^2)\left(\frac{u_e^2 + 2(1-\lambda)}{2\alpha_1 - \lambda}\right)} \tag{52}$$

Finally, once the entry velocity and the corresponding flight path angle is found, u2 non-dimensionalized velocity is found from which we can determine the ΔV required for the maneuver.

$$u_2 = \sqrt{u_e^2 + 2(1-\lambda)} \tag{53}$$

$$\Delta V = \sqrt{(\frac{\mu}{r_D})}(u_1 - u2) \tag{54}$$

F. Variational Analysis

To determine the heating rates and the total integrated heating loads of the vehicle, the Sutton-graves relations given by equation 55 is used to determine stagnation point heat curves which is then integrated using trapezoidal integration scheme to find the integrated heat load.

$$\dot{q} = k\left(\frac{\rho}{r_n}\right)^{0.5} V^3 \tag{55}$$

The changes in velocity, flight path angle, and beta are specified in percentage deviance from the original mission initial conditions, while the LD and sigma are specified together in ratios and degrees. A total of three different variations in parameters can be run to determine the results.

G. Monte-Carlo Analysis

The Monte-Carlo Analysis on the of the reentry trajectory is developed by adding random Gaussian error of 3σ error bounds to the initial entry velocity, flight path angle, latitude, and longitude, to then determine the landing ellipse. The error bounds used in the simulation is summarized in table 3.

Table 3 3-σ Error Bounds for Entry Parameters

Parameter	3-σ Error Bounds
V_e	$\pm 0.3 km/s$
γ	$\pm 0.01^0$
ϕ	$\pm 0.09^0$
θ	$\pm 0.09^0$
ρ	$\pm 0.01 kg/m^3$

Additionally, for the case of air density, the random error are added throughout the entire descent at each time step, this is to simulate the uncertainty in the density model itself similar to the GRAM-95 model, where the 3-sigma bounds are linearly lowered between the altitudes of 70km to 30km as the density is more steady at lower altitudes.

H. Lift and Bank Modulation Analysis

To determine the effects of Lift and Bank angle on the trajectory of the vehicle, specifically, the deceleration profile, cross-range, and down-range, the user can specify three cases of angle of attack of the vehicle and the bank angle to be analyzed. Equation 56 is used to determine s using which the downrange distance S is calculated using 57 through trapezoidal integration method, similarly using 58 is used to determine the cross range of the vehicle for the three diferent cases. These steps are performed as a part of the post processing steps after the numerical integration. This analysis is only available if the non-planar equations of motion are used since the cross range is a function of the azimuth angle.

$$\frac{ds}{dh} = \frac{1}{\sin(\gamma)} \tag{56}$$

$$\frac{dS}{ds} = \cos(\gamma) \tag{57}$$

$$\frac{dl}{dS} = \sin(\psi) \tag{58}$$

I. Simulation Setup

1. Stardust Entry Reconstruction

To verify and test the tool and its capabilities, the stardust mission is first used as a test case to verify the validity of the solver to generate the reentry trajectory given the entry initial conditions and vehicle geometry. Additionally, given an initial elliptical orbit conditions, the entry corridor flight-path angles, delta-V, and the entry velocity will also be solved for, it is important to note that stardust enters from a hyperbolic direct-entry, therefore would have slightly varying results for deorbiting results. Finally, for variational analysis of the entry trajectory, the peak-heating rate, and the integrated heat-load at different entry parameter offsets will be solved for to analyze the fluctuations in heating.

The Stardust vehicle is an axis-symmetric blunt-nose sphere cone with the geometric parameters and the estimated coefficients summarized in the table 4 below. The Vehicle reentry conditions and the initially elliptical orbit and nmax constraints used are summarized 5. The parameters are adopted from the following reference papers [10][11].

Table 4 Stardust Vehicle Geometry

Parameter	Value
m	46 kg
r_n	0.2202
r_c	0.4064
δ_c	60^o
C_{Pmax}	2
C_L	0
C_D	1.5183
A	0.5189
α	0

Table 5 Stardust Mission Parameters

Parameter	Value
β	58.38 kg/m^2
V_e	12.791 km/s
h	125 km
γ_e	8 deg
ψ	96 deg
ϕ	41.59 deg
θ	236.65 deg
r_p	6771 km
e	0.8
ν	180°
n_{max}	32.71 g

For the purposes of verification of the simulation and results of the tool, the Stardust simulation results from the reference paper [10] is used. The data points from the altitude-time and velocity-time plots are first digitized [12] then interpolated to then plot velocity-altitude graphs for comparison. To determine the peak deceleration, altitude at peak deceleration, and velocity of peak deceleration. First the interpolated velocity is numerically differentiated, normalized by gravitational constant and the max is found and its corresponding altitude and velocity it occurs at.

2. Viking Entry

To verify the working of the tool for another planetary mission. The Viking mission to Mars is used for comparison[2], this specifically because multiple references are available for verification. The Vehicle geometry as well as the entry conditions for this simulation is summarized in table 6 and have been adopted from the follosing reference papers [2].

Table 6 Viking Mission Parameters

Parameter	Value
m	930 kg
r_n	0.8763
r_c	1.753
δ_c	70 deg
$C_{p_{\max}}$	2
α	-11.2
β	57.2 kg/m^2
C_L	0.2895
C_D	1.6849
V_e	4.7 km/s
h_e	120 km
γ_e	17.6 deg

IV. Results & Discussion

A. Stardust Trajectory

The altitude vs. velocity simulation results is shown in figure 3. It can be seen that both simpler Planar EOM as well as the Non-planar equations of motion closely follows the trajectory results from the reference paper [10] that did a similar simulation with the same entry conditions and parameters.

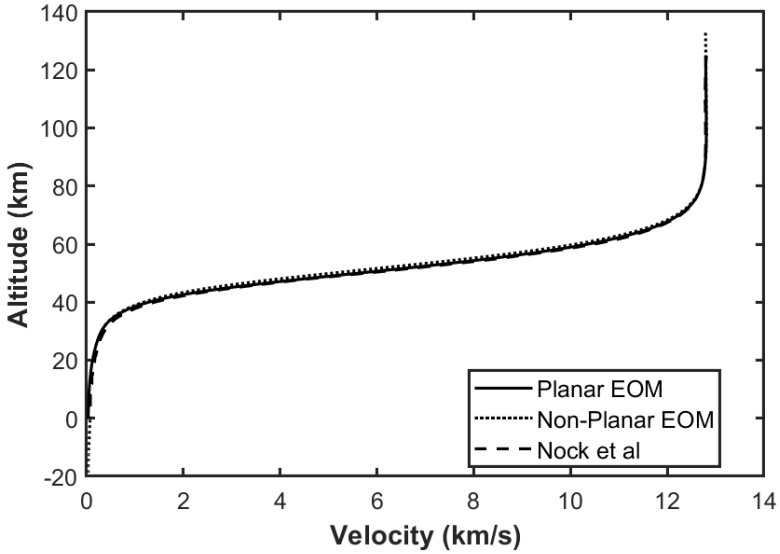

Fig. 3 StarDust Altitude Vs. Velocity

For the stagnation point heating rates, both the planar and Non-planar Equations of motion produced an over-approximation using the Sutton-Graves relations, this is due to the fact that the heating coefficient used by the reference paper [10] is different in comparison to the one used in the simulation from this project. Also there is a slight disparity in the prediction time of the peak heat rate this is because of the slight difference in time of max velocity as seen from 4 as well as the different density models that was used in the reference paper that went into predict the heating rates.

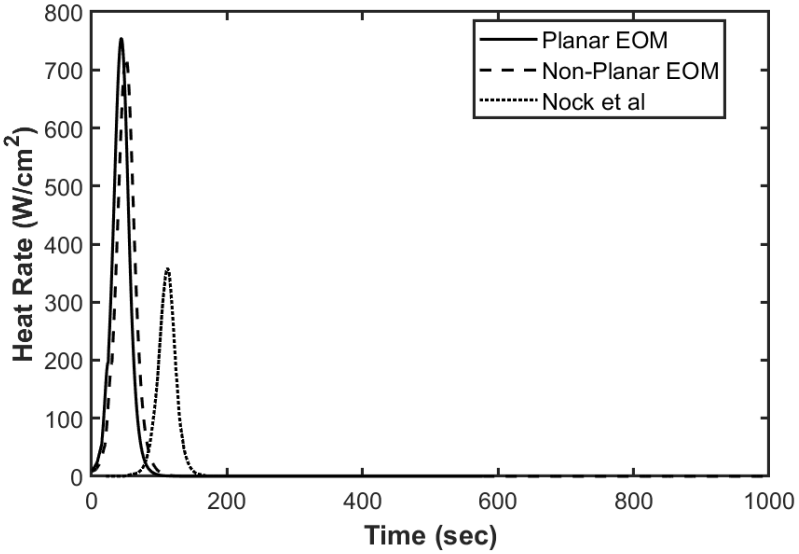

Fig. 4 StarDust Heat Rate Vs. Time

Solving for the de-orbit parameters entering from an orbit of 400km periapsis altitude and 0.8 eccentricity, the entry velocity and flight path angle, as well as the flight path angle corridor for reentry is summarized in table 7. It is important to note that the actual Stardust mission reenters the atmosphere directly from a hyperbolic trajectory unlike in this testing simulation causing a slighlt higher entry velocity in the results obtained, as a form of verification, the Stardust mission reentered at a velocity of 12.79km/s [11] which is near the 10.5km/s prediction from our solver. Additionally, the actual flight path angle from the stardust mission, 8 deg, [10]lies within the flight path angle corridor predicted by this tool in order to satisfy the max deceleration constraint.

Table 7 Estimated Deorbit Parameter and Trajectory Results

Parameter	Value
V_e	10.516 km/s
ΔV	0.0219 km/s
$\gamma_{undershoot}$	4.86^0
γ_e	7.06^0
$\gamma_{overshoot}$	9.26^0

The peak deceleration and the heating results are similarly compared with the interpolated data from the reference paper [10] are tabulated in table 8. The peak deceleration, the peak deceleration velocity and altitude are nearly identical with minor deviations due to errors in digitization of the plots and the errors accumulated from discrete time trapezoidal integration. The peak heat rate and the integrated heat loads are not identical, as explained previously, is due to the use of a different heating rate coefficient in the reference paper in the Sutton-grave relation.

Table 8 Peak Deceleration and Heating Comparison

Parameter	Result	Nock et al
n_{max} (gs)	34.36	33.79
$h_{n_{max}}$ (km)	55.02	54.2
$V_{n_{max}}$ (km/s)	8.34	8.11
$\dot{q}_{max}$ (W/cm^2)	754.12	358.43
q_{max} (J/cm^2)	22343.13	11114.51

For the purposes of analyzing the effect of the variation in entry conditions as well as a banking and lifting entry of the vehicle on the atmospheric heating, the entry parameters were varied accordingly and the heating rates and the total heat loads are summarized in table 9 give below. From the table of values in 9 the steeper, and faster the atmospheric entry becomes, predictably the higher the peak stagnation point heating rate and total integrated heat load, for verification purposes as seen from [13], identical behavior in the heating rates are seen when increasing flight path angle, ballistic coefficient, and entry velocity. For the case of Lifting and Banked entry, there's only a slight decrease in the heat rates and the loads with an increasing Lift to Drag ratio. Figure 5 illustrates the effects of the Lifting and banked entry.

Table 9 Parameter Values with Heating Rate and Heating Load

Parameter	Value	Heating Rate (W/cm^2)	Heating Load (J/cm^2)
V_{e1} (km/s)	10.87	492.20	15313.58
V_{e2} (km/s)	12.15	658.64	19839.38
V_{e3} (km/s)	13.43	858.57	25012.10
y_{e1} (deg)	6.80	622.28	26997.49
y_{e2} (deg)	7.60	715.73	23517.26
y_{e3} (deg)	8.40	788.74	21379.30
$\beta_1(kg/m^2)$	43.50	663.97	18955.34
$\beta_2(kg/m^2)$	53.43	725.67	21261.27
$\beta_3(kg/m^2)$	63.35	781.12	23385.10
$L/D_1, \sigma_1$	$0.10, 30^0$	730.73	24288.44
$L/D_2, \sigma_2$	$0.15, 45^0$	725.63	24982.22
$L/D_3, \sigma_3$	$0.35, 60^0$	707.91	29256.01

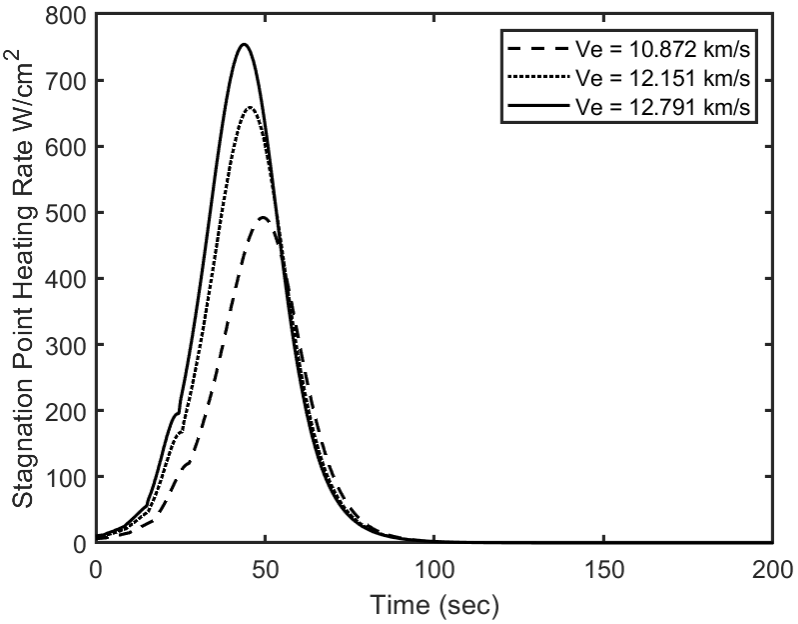

Fig. 5 Stagnation point heat rates for lift and banked entry

To determine the effects of lift and bank modulation on the downrange, cross range and peak deceleration, peak deceleration and altitude, three different cases are studied by varying the angle of attack, thus varying the L/D ratio, and the bank angle. The results for the three cases are summarized in table 10. With increasing alpha and bank angle, the downrange and cross-range distances decrease, and the peak deceleration increases about 5g at each case, with peak deceleration altitude and velocity decreasing.

Table 10 Lifting and Bank Modulation effects on downrange, crossrange, and peak deceleration

α (deg)	σ (deg)	Downrange (km)	Cross-range (km)	n_{max} (gs)	h_{nmax} (km)	V_{nmax} (km/s)
3	10	884.85	880.65	34.06	54.11	7.89
5	20	863.64	860.31	35.97	53.28	7.74
10	30	826.85	825.92	41.03	49.85	6.81

The Landing ellipse generated by the Monte Carlo Runs are produced in figure 6 below. It is imperative to note the the final target landing site and the dispersion width do not match the reference paper this is because the original Stardust reference doesn't provide information on the entry latitude and longitude or the error bounds used in the simulation. As a form of verification, the landing ellipse formed by the Monte Carlo runs are identical in shape, formation, and dispersion as that of the one provided in the reference paper[11].

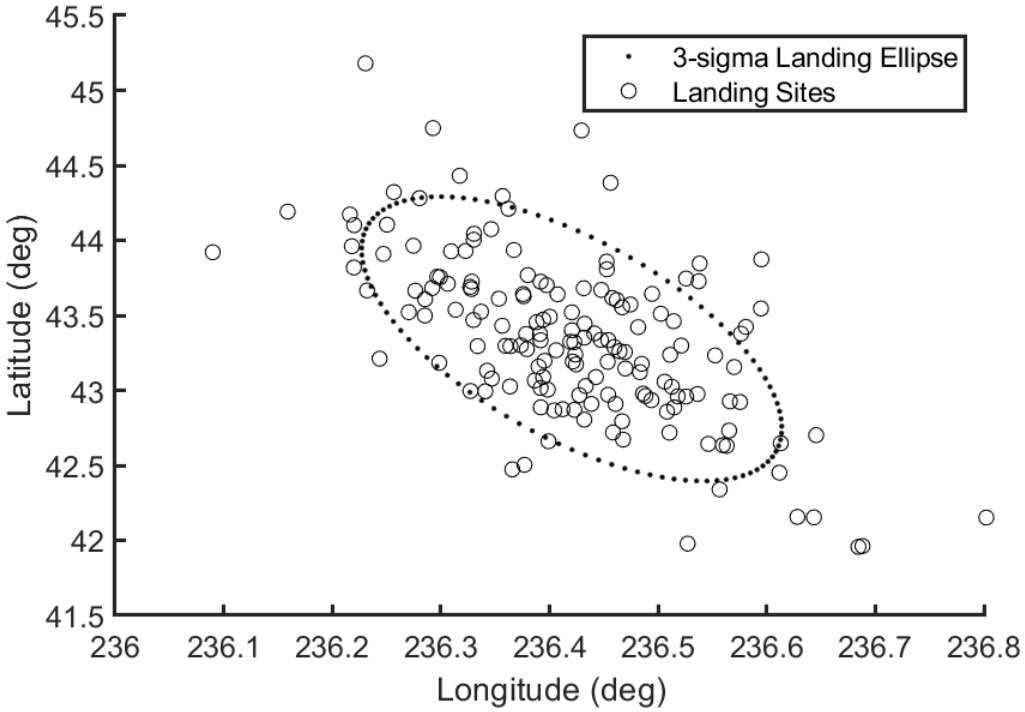

Fig. 6 Monte Carlo Analysis Landing Ellipse

B. Viking Trajectory

The viking entry trajectory is compared to the following reference paper [2]. From figure 7, the Altitude vs. Velocity plot closely match the reference trajectory with minor deviations, this is due to the use of different reference to find the entry conditions for the entry vehicle [2].

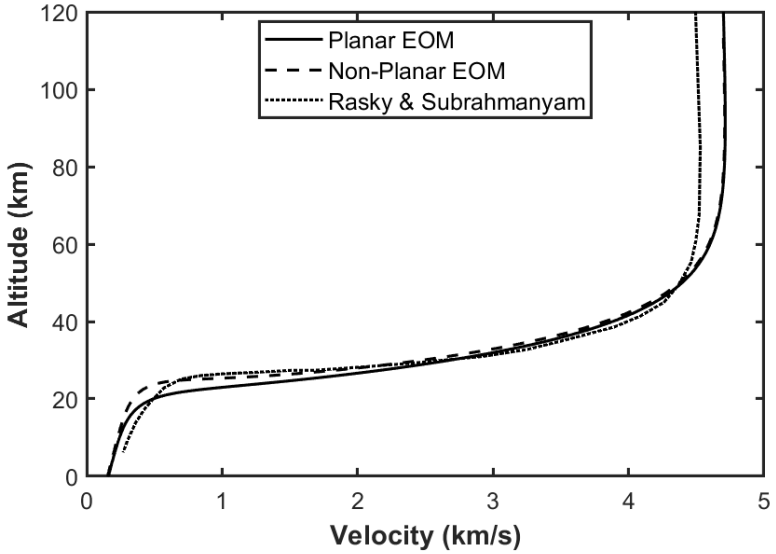

Fig. 7 Viking Trajectory Altitude Vs. Velocity

Similar to the results form the Stardust simulation case, the sutton-graves equation produces a slightly higher over-estimation of the Peak Heat Rate as seen in figure 8, in this case, the reference paper used a higher fidelty model to calculating the heating that and the reference paper starts at a slightly lower entry velocity than used in out simulation, leading to a shift in the timing of the peak heating.

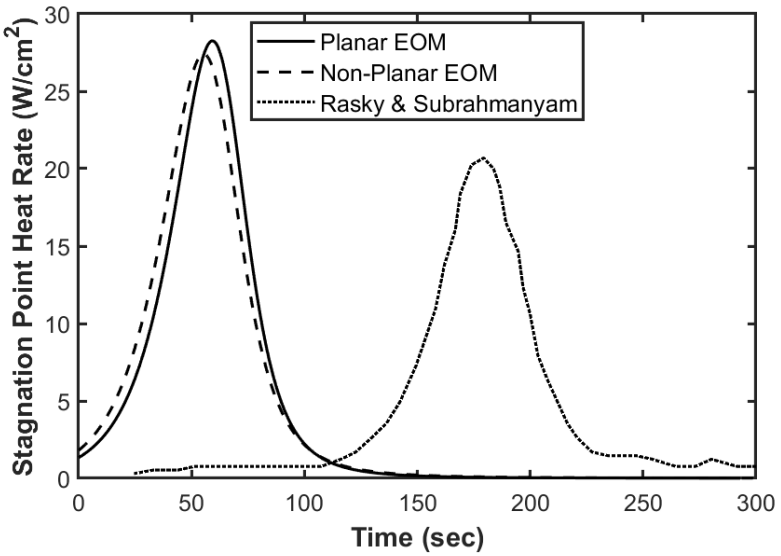

Fig. 8 Viking Stagnation Point Heating Rates

C. Sources of Error and Further Developments

Errors and disparities in the results obtained in contrast to the other reference sources in recreating the trajectories are due to use of the use of higher order integrators that are more accurate in comparison to the simple low order Runge-Kutta 4th order schemes used in this project, as well as discrete integration using trapezoidal rule with fixed time steps acculumate error causing disparities. Additionally, errors in digitizing the plots from the reference papers directly from the graphs themselves causes misalignment errors in the plots. Errors relating to landing ellipse and site determination is due to insufficient information found on the error bounds for the Monte Carlo Runs and the initial landing site.

Overall, this project served as an initial mission analysis that provides insights and a first hand approximation on the entry descent trajectory design and analysis. This can further be improved on by using a higher order, 6DOF, equations of motion, as well as more accurate and updated atmospheric and gravity models, and better integrators that allow for better tolerances. Additionally for the case of deorbit trajectory estimation, the tool can be extended to use estimate the entry parameters for hyperbolic cases as well.

V. Conclusion

This research project successfully developed a mission design tool that simulates atmospheric reentry trajectories and estimates deorbiting parameters for mission design and analysis. The tool, validated using the Stardust and Viking missions, demonstrated effectiveness in predicting entry trajectories and heating rates, performing parameter variational analysis, Lifting and Banking Modulating analysis, as well as Monte Carlo Runs. Although slight discrepancies due to varying atmospheric models, integrator accuracies, errors in digitization, the tool performed well for an initial mission design for first hand approximation. Future enhancements, such as adopting higher-order integrators, upgrading to latest atmospheric and gravity models, and expanding the tool to handle hyperbolic entry cases, are essential. This foundational work paves the way for more accurate and reliable EDL analysis in future planetary missions.

Appendix

A. Main Scripts Breakdown

RUN_SCRIPT.m : Running this script prompts the user with multiple diaglog boxes that the user can input the data accordingly to run their simulation. By default, the entry simulations can be run for Earth, Mars, and Venus, as well as a special case for stardust that has been hard-coded as well. The user can opt to run different analysis as prompted by the tool when the script is run.

For running Stardust Test case and producing resulting the Main_Stardust.m script can be run. Also Plot_Viking.m script for producing results for the viking mission.

On running these script, some sections will take time to compute, and the final results will be plotted in multiple separate windows and displayed in tables in the command window as well. An image below is attached illustrating the output for the Stardust entry case.

CL	0
CD	1.51834878230303
A (m^2)	0.518868458595838
LD	0
B (kg/m^2)	58.388728094868

Solving for Deorbit Parameters please wait....

Results

Ve (km/s)	10.5161460379653
ye (deg)	7.06202351004962
Delta-V (km/s)	0.0219101354235686
ymin (deg)	4.864
ymax (deg)	9.26

Results

nmax (gs)	34.3603483127805
hnmax (km)	55.0215788525257
Vnmax (km/s)	8.34467546403426
qdotmax (W/cm^2)	754.116920043219
qintmax (J/cm^2)	22343.1315154597

	Parameter Value	Heating Rate (W/cm^2)	Heating Load (J/cm^2)
Ve1 (km/s)	10.87235	492.201335658172	15313.5782264595
Ve2 (km/s)	12.15145	658.643388975017	19839.375654862
Ve3 (km/s)	13.43055	858.567728434527	25012.1009587821
ye1 (deg)	6.8	622.281834366725	26997.4866354208
ye2 (deg)	7.6	715.729056298118	23517.2604902425
ye3 (deg)	8.4	788.738121273742	21379.2956960449
B1 (kg/m^2)	43.4996024306767	663.974070354926	18955.3428065078
B2 (kg/m^2)	53.4256862068042	725.668836108071	21261.2703807205
B3 (kg/m^2)	63.3517699829318	781.121993338898	23385.1019488504
LD1/Bank1	0.1	730.733127429939	24288.435585655
LD2/Bank2	0.15	725.629467027419	24982.218479563
LD3/Bank3	0.35	707.90813971974	29256.0131900623

Fig. 9 MATLAB results

alpha (deg)	sigma (deg)	Downrange (km)	Crossrange (km)	nmax (gs)	hnmax (km)	Vnmax (km/s)
3	10	884.853035190858	880.650906148435	34.0579934119828	54.1132869221969	7.88631281083753
5	20	863.638501403956	860.307057586013	35.9740790246626	53.2758588743955	7.73752080251318
10	30	826.847400951008	825.924774319203	41.025249978368	49.8474359053094	6.81174116682767

Fig. 10 MATLAB results 2

B. Helper Function Scripts Breakdown

Atmospheric Models: "Atm_exponential_model.m" and "Atm_1962_1976_model.m"
- Gravity Models: "Grav_J2_model.m" and "Grav_inverse_model.m"
Geometry Models: "Geom_conic_model" and "Geom_biconic_model.m"
Equations of Motion: "EOM_3DOF_planar.m" and "EOM_3DOF_nonplanar.m"

References

[1] Banke, J., "Apollo 11's Return to Earth Rooted in Aeronautics Research," *NASA*, 2019. URL https://www.nasa.gov/feature/apollo-11s-return-to-earth-rooted-in-aeronautics-research.

[2] Subrahmanyam, P., and Rasky, D., "Entry, Descent, and Landing technological barriers and crewed MARS vehicle performance analysis," *Progress in Aerospace Sciences*, Vol. 91, 2017, pp. 1–26. https://doi.org/10.1016/j.paerosci.2016.12.005, URL https://ntrs.nasa.gov/citations/20200002997.

[3] NASA, "Aerodynamic Planeuvering Hypersonic Flight Mechanics," Tech. rep., NASA Grant NAG 2-457, 1988. Period of Performance: June 1, 1987 - September 30, 1988.

[4] Sutton, K., and Graves, R., "A General Stagnation-Point Convective-Heating Equation for Arbitrary Gas Mixtures," *Journal of Spacecraft and Rockets*, Vol. 7, No. 4, 1970, pp. 543–548. https://doi.org/10.2514/3.30122.

[5] Dec, J., "8.1; Entry Corridors, Entry Heating Basics," *AE6355 Lecture Notes*, 2024.

[6] NASA, "U.S. Standard Atmosphere, 1962: ICAO Standard Atmosphere to 20 Kilometers, Proposed ICAO Extension to 32 Kilometers, Tables and Data to 700 Kilometers," , 1962. URL https://ntrs.nasa.gov/citations/19630003300.

[7] NASA, "U.S. Standard Atmosphere, 1976," Tech. rep., NASA Technical Reports Server (NTRS), 1976. URL https://ntrs.nasa.gov/archive/nasa/casi.ntrs.nasa.gov/19770009539.pdf.

[8] Cheng, M., Tapley, B. D., and Ries, J. C., "Deceleration in the Earth's oblateness," *Journal of Geophysical Research: Solid Earth*, Vol. 118, 2013, pp. 740–747. https://doi.org/10.1002/jgrb.50058, URL https://grace.jpl.nasa.gov/data/get-data/oblateness/.

[9] Regan, F. J., and Anandakrishnan, S. M., *Dynamics of Atmospheric Re-Entry*, American Institute of Aeronautics and Astronautics, Washington, D.C., 1993.

[10] Medlock, K. L. G., Lyne, J. E., and Nock, K. T., "Hypersonic Planetary Aeroassist Simulation System Validation," *Journal of Spacecraft and Rockets*, 2016. URL https://www.gaerospace.com/projects/HyperPass/HyperPass.html.

[11] Desai, P. N., and Qualls, G. D., "Stardust Entry Reconstruction," *5th International Planetary Probe Workshop*, NASA Langley Research Center, 2007. URL https://ntrs.nasa.gov/citations/20080010667.

[12] Automeris LLC, "Copyright 2024 Automeris LLC, California, USA," https://automeris.io/, 2024. Email: plots@automeris.io.

[13] NASA, "Aerothermodynamics Course," , 2012. URL https://tfaws.nasa.gov/TFAWS12/Proceedings/Aerothermodynamics%20Course.pdf, tFAWS 2012 Proceedings.